The San Francisco Bay Area –

APPENDICES - Documentation for 2003 Mapping Updated in 2010

Association of Bay Area Governments Earthquake and Hazards Program

NOTE: All references in this document are located in the main "On Shaky Ground" report section on 1995 report references.

Authors of "On Shaky Ground" report and these appendices:

Jeanne B. Perkins – Consultant; former Earthquake Program Manager, Assoc. of Bay Area Governments
John Boatwright -- Geophysicist, U.S. Geological Survey

TECHNICAL APPENDIX A-- SOURCE MODEL FOR MAPPING INTENSITIES FOR LARGE STRIKE-SLIP EARTHQUAKES

Introduction

Three aspects of earthquake sources are critical for estimating ground motions in the near and intermediate field of large strike-slip earthquakes:

- the scaling of ground motions with source size
- the finite extent of the earthquake source
- the focusing of seismic radiation, or directivity

The first aspect is the scaling of ground motion with source size, that is, how much does the ground motion increase as the size, or the magnitude, of the earthquake increases? The usual course of seismological research is to use the information from more frequent moderate earthquakes to predict the effects of rarer large earthquakes. The methods used for these extrapolations are known as scaling relations. Because there are relatively few recordings for great earthquakes, the empirical scaling relations for these earthquakes are poorly determined.

The second aspect is the effect of the physical extent of the source, or the source finiteness, on the radiated ground motions. In general, earthquakes are areally distributed, that is, an earthquake radiates seismic waves from those parts of the fault area that slip during the rupture process. The physical structure of the problem implies that ground motions must saturate, or reach a maximum, near the fault surface. However, so few recordings have been obtained near the faults of large earthquakes that this saturation cannot be readily discerned in the data (Joyner and Boore, 1981).

The third aspect is the focusing of seismic energy, or directivity, resulting from the geometry of the earthquake rupture. If we know the rupture geometry, it is possible to determine reasonable estimates of the directivity. For example, the effect of directivity for a long strike-slip earthquake can be bounded by the limiting cases of the rupture nucleating at either end. In general, however, estimating the effect of directivity for the rupture of a fault segment requires taking an expectation over the set of possible hypocenters and rupture histories.

The source model used in this report contains source scaling, source finiteness, and directivity. Although the fault is buried, the motions near the fault trace are very strong. This near-fault motion results from the combination of a partially updip rupture and the amplification of ground motion associated with the velocity structure of the fault itself. Combining this near-fault intensity with strong horizontal directivity yields a source model that fits the 1906 intensities as a function of distance from the fault trace, as well as fits the intensity patterns for the 1989 Loma Prieta and 1984 Morgan Hill earthquakes. Further work is planned during 1995 to apply this technique to earthquakes on thrust faults such as the 1994 Northridge earthquake, and to test the model using strong ground recordings of the 1995 Kobe, the 1994 Northridge, and the 1992 Landers earthquakes.

Background

To consider these three aspects of the seismic source, it is useful to discuss how they are addressed in the three source models that have been used for mapping intensity and ground motion. The three models we will discuss are the attenuation relationship determined for the 1906 earthquake by Borcherdt et al. (1975), the model and program by Evernden (1991) derived from the models and analyses in Evernden et al. (1981) and Evernden and Thompson (1988), and the source model that forms the basis for the regressions of Joyner and Boore (1981) and Boore et al. (1993). While Joyner and Boore (1981) did not make ground motion or intensity maps, their regression models for peak ground acceleration (PGA), peak ground velocity (PGV), and more recently, for the pseudo-velocity response spectra (Boore et al., 1993), have been used by other researchers to map ground motions.

Borcherdt et al. (1975) derived an attenuation law for the San Francisco intensity scale as a function of the distance normal to the San Andreas fault in the 1906 San Francisco earthquake. The set of intensities that they fit were obtained on a single rock-type, the Franciscan assemblage. Their "observed" intensities are shown in Figure 1. These researchers also estimated differences in the observed intensity between the Franciscan formation and the other surficial rock-types in the area. They then mapped the 1906 intensities, with corrections for these rock-types, as a function of distance from the San Andreas and Hayward faults, to estimate the maximum intensity expected for large earthquakes on these two faults.

Borcherdt et al. (1975) fit the intensity as a function of the inverse of the distance from the surface trace of the fault, motivated by the very large intensities observed within 2 km of the fault trace. This clustering of the strongest intensities along the fault trace clearly distinguishes their method for estimating intensity from the models of Evernden et al. (1981) and Joyner and Boore (1981) where the seismic source is buried, and expected ground motions and intensities do not peak near the fault trace.

The 1906 San Francisco earthquake approximates a limiting case for considering source finiteness, in that the 1906 rupture extends far beyond the sites in San Francisco and the Bay Area. Borcherdt et al. (1975) propose no scaling to estimate the ground motion for smaller earthquakes. There is no explicit directivity in the model because no intensities were observed beyond the ends of the 1906 faulting.

Perkins (1983, 1987a, 1987b, and 1992) has applied this attenuation in an effort to model various earthquakes that have occured or are anticipated to occur in the Bay Area, including the 1989 Loma Prieta earthquake, by using the closest distance to the rupture trace in the place of the normal distance from the fault. In the first three reports, Perkins scales the intensity by dropping each intensity by one unit for **M** ≈ 7 events. Perkins (1992) eliminated this scaling.

Evernden (1991) uses a set of empirical relations among fault length, magnitude, and radiated energy as his scaling relations. He subdivides his finite length source into a set of subsources and sums the radiation from these subsources using a unique summation rule. His summation procedure yields a distributed source so that the intensities saturate, that is, reach a limiting value in the near-field. His fault and its subsources are buried, so the ground motions predicted along the fault trace are moderate.

To compare Evernden's attenuation with that of Borcherdt et al. (1975), we have modeled the 1906 earthquake using the computer program of Evernden (1991) and assuming an intensity correction of $\Delta I = -2.2$, Evernden's correction for Franciscan sandstone. Evernden's predicted intensity is plotted as a shaded line. His predicted curve significantly underestimates the observed 1906 intensities within 5 km of the fault trace. This underestimate results from both the depth of Evernden's source and the lack of directivity in his model.

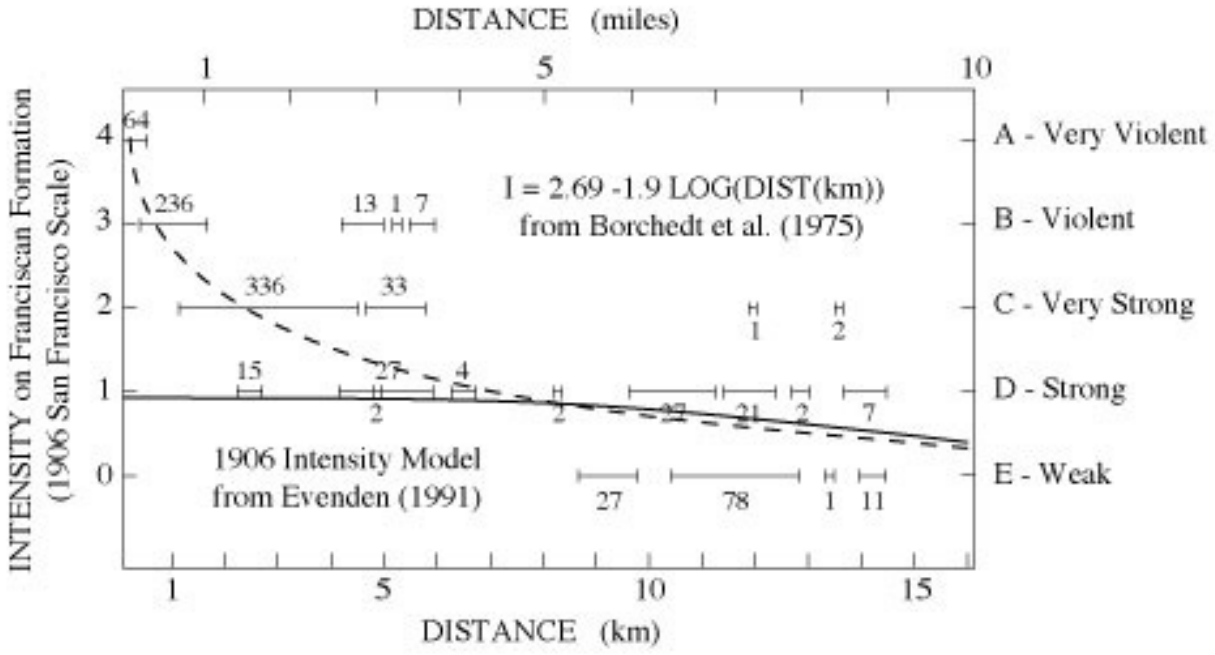

FIGURE 1. San Francisco intensity, observed at sites on Franciscan assemblage, and plotted as a function of distance normal to the San Andreas fault (revised from Borcherdt et al., 1975). The dashed line shows the fit to these intensity estimates obtained by Borcherdt et al. (1975). The solid line shows the intensities for the 1906 earthquake determined by Evernden (1991) for rock-types with the same amplification as Franciscan sandstone. San Francisco intensities A-E were assigned the values 4-0 in Borcherdt et al. (1975).

The Joyner and Boore (1981) model is the seismic source model most widely accepted and understood by engineers. The scaling with seismic moment for each measure of ground motion is obtained empirically. Their model is essentially a point source, but they incorporate the extent of the earthquake by using the closest distance to the surface projection of the rupture area as the measure of source-receiver distance. They assume that all the faults are buried at a single depth, $h = 7.0$ km, estimated by regressing the entire data set. Because the source is not distributed over a set of subsources, as in Evernden's (1991) model, the ground motions predicted near the fault trace are moderate to strong. There is no explicit directivity in their model.

General Model Approach

The modeling approach used in this research has three parts. First, we derive an analytical model that incorporates the three aspects of the earthquake source (scaling, finiteness, and directivity) described in the introduction to estimate the ground motion parameter of the average acceleration spectral level. This parameter has units of velocity rather than acceleration and resembles peak velocity more than peak acceleration. The model is described in the next two sections.

Second, we calibrate this model by fitting the attenuation curve determined by Borcherdt et al. (1975) for the 1906 earthquake. This fitting anchors the relationship between the average acceleration spectral level and intensity. As a second constraint, we consider the variation of intensity with amplification determined by Borcherdt et al. (1975). Our analytical model provides a satisfactory fit to both of these relationships.

Finally, the resulting intensity model was tested for both the 1989 Loma Prieta and the 1984 Morgan Hill earthquake. This second testing process was complicated by the model output (in acceleration power spectral level) being calibrated using the San Francisco intensity scale, which is no longer commonly used. Fitting the observed damage for the 1989 Loma Prieta earthquake is critical, because this earthquake is an analog to most of the scenario events mapped in this report. It also exhibited significant directivity that can be used to statistically constrain the amount of directivity that we then incorporate into the scenario earthquakes. Fitting the damage for the 1984 Morgan Hill earthquake tests the source scaling characteristics of the model. ***Those readers who are not interested in the mathematical derivation of the model may be interested in this section on "Testing..." beginning on page 46.***

A Composite Source Model

The critical components of the composite source model are the subevents, or areal fault elements, distributed at depth below the fault trace. These subevents can be distributed either in a line along strike, at a single depth, or over the area of the rupture surface. Clearly, the linear source model is computationally simpler, and it is reasonable to consider whether an areal source is required to model the relatively large strike-slip earthquakes anticipated for the Bay Area. A sufficiently general source model should be able to accommodate either description, however.

The subevents have two important characteristics. First, they radiate seismic energy (or acceleration spectral amplitude) in azimuthal patterns that exhibit directivity, or a range of possible directivities. Incorporating directivity constitutes the clearest break with the source models used for previous hazard maps. However, we feel that directivity is an important characteristic of almost every intensity pattern observed for large strike-slip earthquakes.

The directivity functions of the subevents should be derived from the rupture process of the earthquake being modeled. If we know the rupture geometry, that is, the rupture direction, ϕ_i, for a subevent or areal element of the fault, we can use the directivity function of Ben-Menahem (1961),

$$D(\phi_i) = \frac{1}{1 - \frac{v}{\beta}\cos\gamma_i} \qquad \textit{Equation 1}$$

where v is the rupture velocity, β is the shear wave velocity, and γ_i is the angle between the takeoff direction of the shear wave from the i th subevent and the rupture direction ϕ_i as shown in Figure 2.

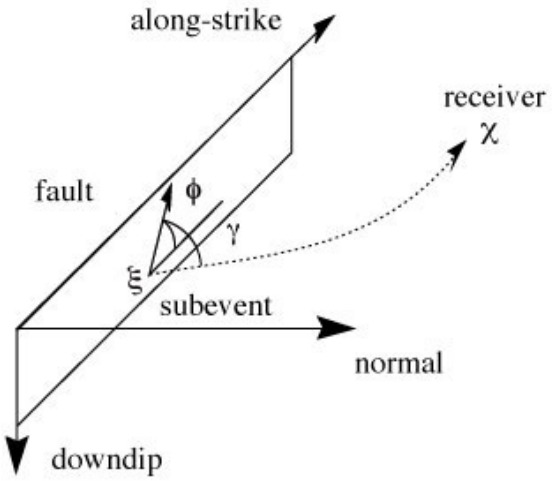

FIGURE 2. A schematic diagram of the relevant angles necessary for the analysis of directivity. The rupture direction is assumed to be partly along strike and partly updip. The angle ϕ is the angle between the rupture direction and the along strike direction. The angle γ is the angle between the rupture direction and the takeoff angle of the wave observed at *x*.

If we do not know the rupture geometry, but can estimate the probability $P(\phi_i)$ of the rupture direction at *i*, then we should use the expected directivity D_i, as

$$(D_i)^{\lambda} = \int \frac{P(\phi_i)d\phi}{(1-\frac{v}{\beta}\cos\gamma_i)^{\lambda}}$$

Equation 2

in the place of the directivity function. The exponent λ is determined by the coherence of the motions being summed, according to the summation convention discussed below.

The second characteristic of the subevents is that the acceleration power spectrum radiated by a subevent is proportional to $\Delta\sigma^2\Sigma$, where $\Delta\sigma$ is the dynamic stress drop and Σ is the fault area of the subevent. Boatwright (1982) derives the following relationship for the average acceleration spectral level radiated from the *i*th subevent at ξ to a receiver at *x* :

$$\left|\ddot{u}_i(x)\right| \propto \frac{D_i\ \Delta\sigma\ \Sigma^{1/2}}{r(\xi,x)}$$

Equation 3

where the geometrical attenuation term $r(\xi,x)$ is assumed to be adequately approximated by the distance between the subevent and the receiver. The average acceleration spectral level is modelled as an average of the Fourier amplitude spectrum of the ground acceleration for frequencies above the corner frequency of the earthquake (Boatwright, 1982). Equation 3 is appropriate for the frequencies of ground motion that can damage most small to moderate-sized structures (0.3 to 3 Hz) for **M**=7 earthquakes, but may overestimate the average acceleration spectral level for **M**<6.5 earthquakes in the direction of rupture. Housner (1970) shows that the undamped velocity response spectrum approximates the Fourier spectrum of the ground acceleration. We note that the average acceleration spectral level has units of velocity rather than acceleration; it scales like peak ground velocity rather than peak ground acceleration.

An important element of the model is the method by which the subevent radiation is summed to estimate the earthquake ground motion. If the wave forms radiated by the subevents were one-sided pulses that shared the same polarity, the subevent radiation would sum coherently as

$$\left|\ddot{u}\right| = \sum_i \left|\ddot{u}_i\right|$$

Equation 4a

commensurate with the exponent $\lambda = 1$. This method of summation is only appropriate for the lowest frequencies radiated by an earthquake, however. The acceleration radiated by the subevents has pulses with both positive and negative polarities that integrate together to zero. That is, the ground stops moving after an earthquake or the subevent of an earthquake. Under this condition, the radiation should be summed incoherently as

$$\left|\ddot{u}\right|^2 = \sum_i \left|\ddot{u}_i\right|^2$$

Equation 4b

commensurate with the exponent $\lambda = 2$ in the directivity function in equation 2. Evernden (1981) uses the exponent $\lambda = 4$ in his summations.

The incoherent summation $\lambda = 2$ was first motivated by Boatwright (1982) to calculate the far-field acceleration from dynamic ruptures. This method of summation is also commensurate with the assumption of a stochastic or random distribution of source strength. The slip and stress drop distributions of large earthquakes appear strongly heterogeneous, rather than uniform. In general, however, we have little knowledge of the spatial variation of the stress drop on a fault surface. For the fault models used in this report, we assume that the stress drop is constant, or uniform, over the rupture area. The source heterogeneity is more readily incorporated using the incoherent sum in equation 4 than by summing over different realizations of a heterogeneous rupture process.

By using an integral over the fault instead of a summation over subevents, the average acceleration spectral level can be written as proportional to the integral

$$|\ddot{u}|^2 \propto \Xi^2 = \int \frac{D^2\,\Delta\sigma^2}{r^2}\,d\Sigma$$

Equation 5

where $d\Sigma$ is the incremental fault area and $\Delta\sigma = 1$. To reduce the composite source model to its constituent aspects, it is useful to define integral or fault-average estimates for D and r (retaining the spatially variable stress drop for completeness). These averages are the rms quantities:

$$\left\langle \frac{1}{r} \right\rangle^2 = \frac{1}{\int \Delta\sigma^2 d\Sigma} \int \frac{\Delta\sigma^2}{r^2}\,d\Sigma$$

$$\langle D \rangle^2 = \frac{1}{\int \frac{\Delta\sigma^2}{r^2}\,d\Sigma} \int \frac{D^2\,\Delta\sigma^2}{r^2}\,d\Sigma$$

Equations 6 and 7

Manipulating equation 5 by algebraic substitution and taking the square root of both sides, we obtain the simple form:

$$\Xi = \left\langle \frac{1}{r} \right\rangle \langle D \rangle \left[\int \Delta\sigma^2 d\Sigma \right]^{1/2}$$

Equation 8

This form makes explicit the three aspects of the seismic source discussed in the Introduction. The term $\langle 1/r \rangle$ contains the source finiteness effect, explicitly calculated as the root mean square inverse distance from the fault surface. This term depends only on the spatial extent of the source and the distribution of stress drop. The second term $\langle D \rangle$ contains the effect of directivity or focusing, possibly obtained from an expectation over a set of rupture geometries. The last term $\left[\int \Delta\sigma^2 d\Sigma\right]^{1/2}$ contains a measure of the overall source strength that is independent of the source-receiver geometry and rupture geometry. This last term is the source scaling term.

A Trilateral Rupture Model

In general, the problem of determining the directivity is relatively difficult, requiring an expectation over the set of possible rupture geometries for the fault segment. For large strike-slip faults, however, the predominate directions of rupture propagation are horizontal and updip. The rupture propagates horizontally along strike, either unilaterally or bilaterally, and it propagates updip because of the general increase of seismic velocity with depth; effectively, the faster rupture of the deeper areas of the fault drives the rupture of the shallower fault areas. In addition, the general increase of the stress state with depth implies that ruptures usually start at depth and rupture updip (Das and Scholz, 1983). Figure 3 shows a schematic of the rupture growth on such a fault; the rupture propagates horizontally on the deeper sections and vertically on the shallower sections of the fault.

For such a fault, we approximate the probability for the direction of rupture at each subevent as $P(\phi = 0^\circ, 90^\circ, 180^\circ) = 1/3$. The resulting directivity function is

$$D_i^2 = \frac{1}{3(1-\frac{v}{\beta}\cos\gamma_+)^2} + \frac{1}{3(1-\frac{v}{\beta}\cos\gamma_-)^2} + \frac{1}{3(1-\frac{\upsilon}{\beta}\cos\eta)^2}$$

Equation 9

where v is the horizontal rupture velocity, $\gamma_+ = \pi - \gamma_-$ are the appropriate direction cosines for horizontal rupture in the two directions along strike, υ is the updip rupture velocity, and η is the direction cosine for updip rupture.

For simplicity, all subevents on the fault are assumed to share this same directivity function. Although computationally simple, the trilateral rupture yields an adequate approximation of the expectation over the three most obvious rupture geometries (unilateral, starting at either end of the fault, and bilateral).

To calculate the acceleration spectral level, then, we numerically integrate equation 5 over a line of subsources at the fixed depth of 5 km, between the specified ends of the rupture. The stress drop is assumed to be constant at $\Delta\sigma = 1$, and the trilateral directivity function in equation 9 is used for each subsource. Using a line source to model these large strike-slip faults reduces the integrand $d\Sigma = w d\ell$ where w is the total width of the fault, and $d\ell$ is the incremental length evaluated in the numerical integration. Note that this integration does not require specifiying the time dependence of the rupture process, only its incoherence. The square root of the resulting integral yields the (normalized) estimate of the average acceleration spectral level.

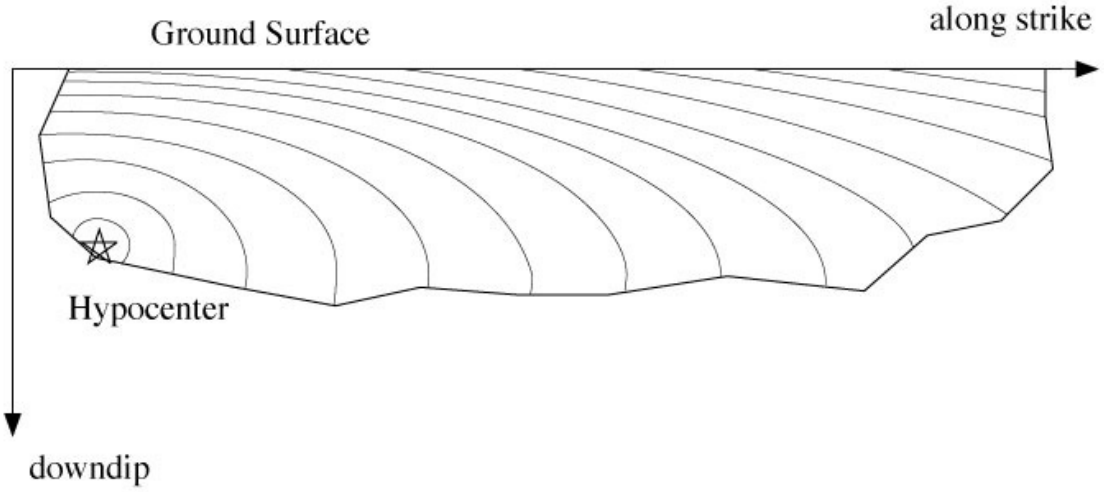

FIGURE 3. A schematic diagram of rupture propagation (plotted as rupture fronts at equal time increments) on a long strike-slip fault embedded in a crustal velocity structure in which the S-wave velocity increases with depth. The faster horizontal rupture of the deepest segment of the fault drives the updip rupture process on the shallower segments.

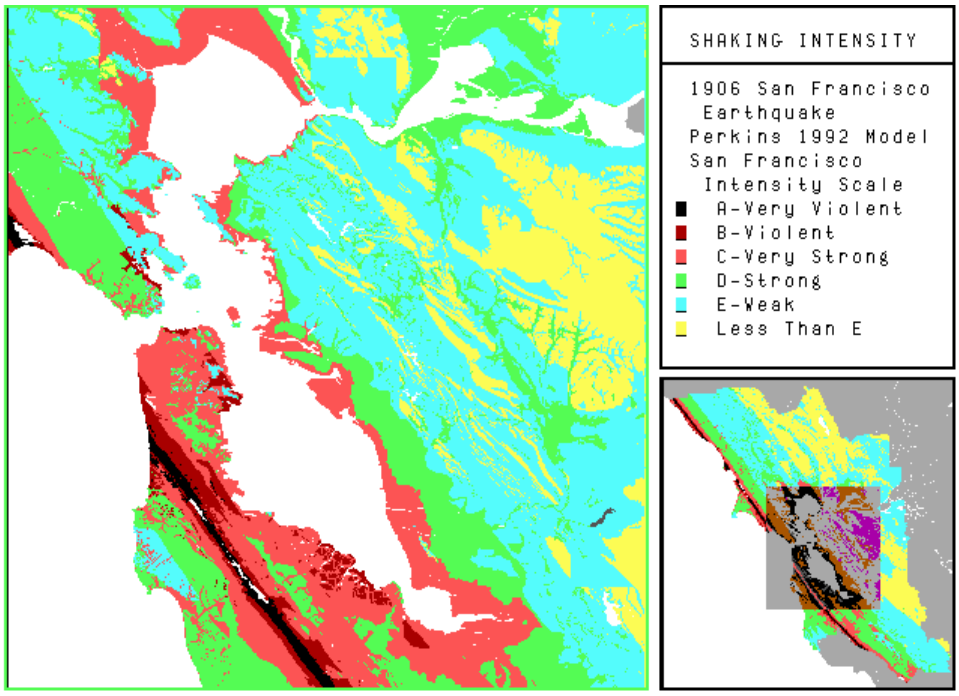

PLATE 1a -- Map showing intensities for a repeat of the 1906 San Francisco earthquake based on the attenuation relationship described in Borcherdt et al. (1975) and used as a model in Perkins (1992) with the intensity increments described in Appendix B.

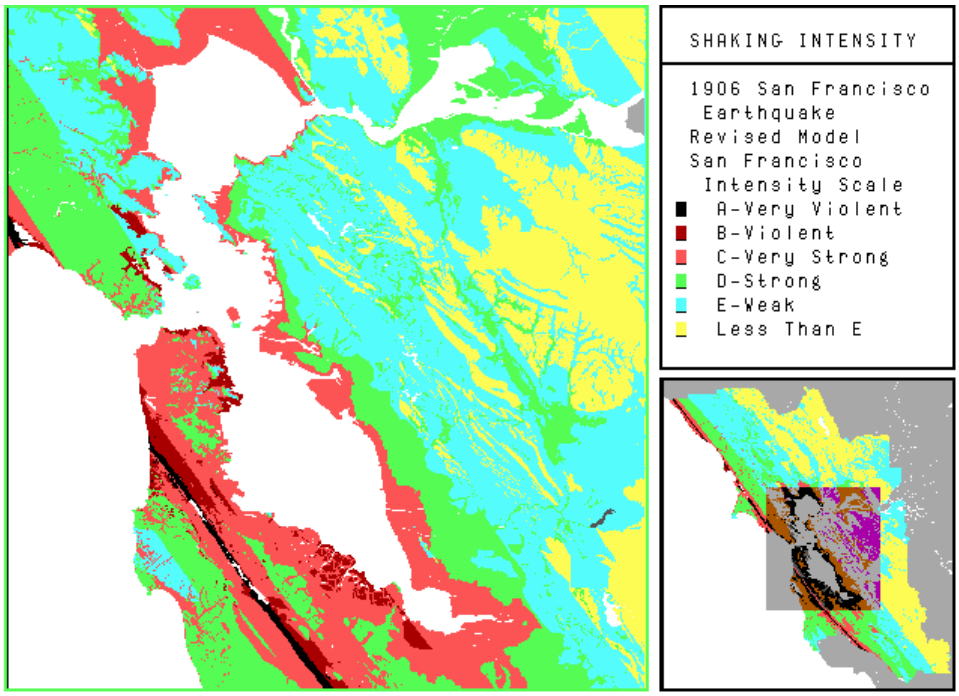

PLATE 1b -- Map showing intensities for a repeat of the 1906 San Francisco earthquake based on the revised relationships described in this Appendix, with the intensity increments described in Appendix B.

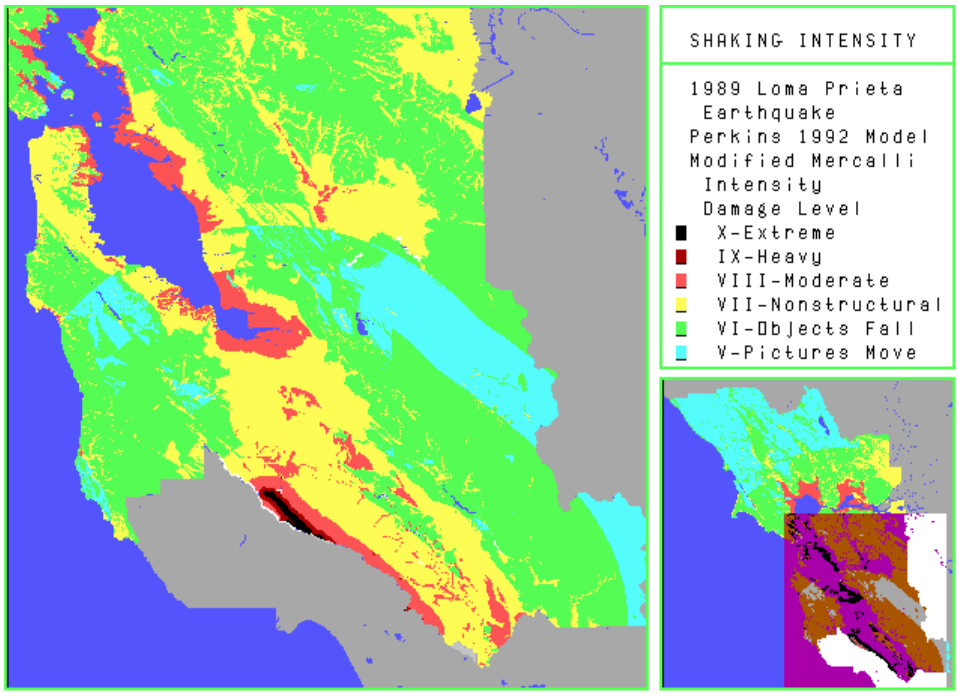

PLATE 2a -- Map showing intensities for a repeat of the 1989 Loma Prieta earthquake based on the model described in Borcherdt et al. (1975) and used as a model in Perkins (1992), with the intensity increments described in Appendix B.

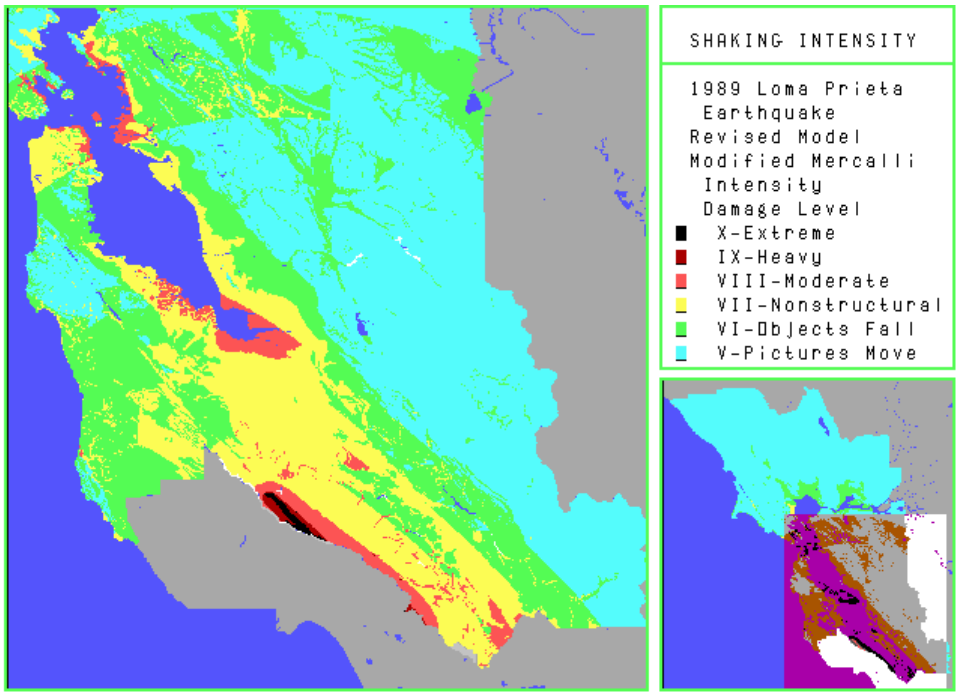

PLATE 2b -- Map showing intensities for a repeat of the 1989 Loma Prieta earthquake based on the revised relationships described in this Appendix, with the intensity increments described in Appendix B.

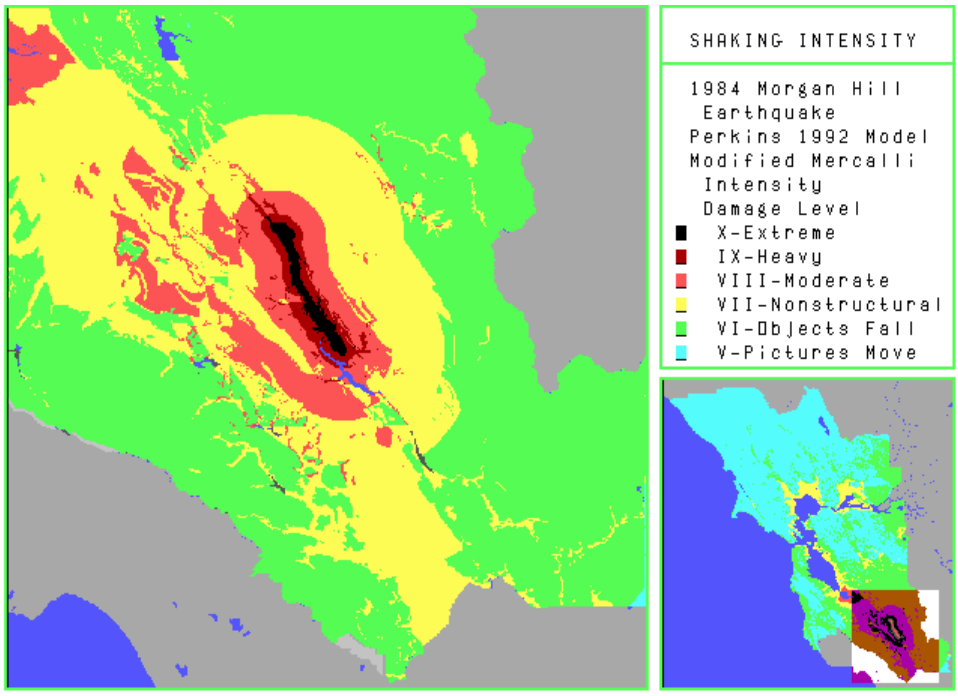

PLATE 3a -- Map showing intensities for a repeat of the 1984 Morgan Hill earthquake based on the model described in Borcherdt et al. (1975) and used as a model in Perkins (1992), with the intensity increments described in Appendix B.

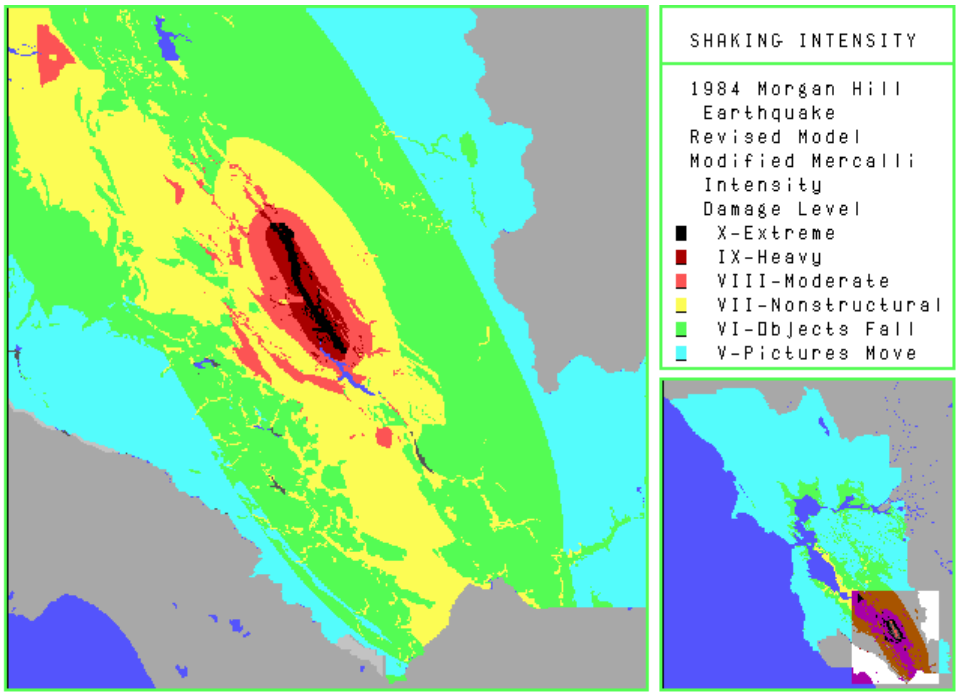

PLATE 3b -- Map showing intensities for a repeat of the 1984 Morgan Hill earthquake based on the revised relationships described in this Appendix, with the intensity increments described in Appendix B.

Calibrating Intensities Normal to the Fault Trace

Before we can apply this model to the problem of predicting intensities, however, we need to calibrate the relationship between intensity and ground motion for large strike-slip faults. We obtain this calibration by fitting the logarithm of the predicted acceleration spectral level for a 400-km-long fault to the intensities plotted in Figure 1 by Borcherdt et al. (1975).

Using the rupture velocities $v = 0.8\beta$ and $\upsilon = 0.95\beta$ in the model, we can fit the level and falloff of the 1906 intensities normal to this fault using the relation,

$$I_{1906} = 1.0 + 3.0\log(\Xi)$$

Equation 10

The fit is plotted in Figure 4. This comparison makes the motivation for using different velocities for the horizontal and vertical rupture processes clear. The ground motions near the trace of the fault are dominated by the updip directivity, that is, the third term in equation 8. It is necessary to use an artificially fast updip rupture velocity to fit the strong intensities observed near the fault in the 1906 earthquake. Even with this high a rupture velocity, the intensities observed closest to the fault are somewhat underestimated by this model. Borcherdt et al. (1975) fit the intensity data as a function of distance both using and not using the data in the immediate fault zone and obtained essentially the same attenuation relationship.

It is possible that the high intensities observed within 2 km of the fault are the result of the low-velocity zone associated with the fault itself. These narrow low-velocity zones act as wave guides for shear waves with periods from 0.3 to 1 s (see Li et al., 1994). The major strike-slip faults in the Bay Area have pronounced low-velocity zones whose widths range from 100 m to 2 km. These low-velocity zones channel and strongly amplify transversely polarized shear waves, the strongest waves radiated by a strike-slip earthquake. A more sophisticated model for the ground motions would incorporate this amplification through a factor that depends on the distance from the fault trace; the updip rupture velocity required to fit such a model to the observed intensities could be as low as $v = 0.8\beta$, depending on the assumed near-fault amplification factor.

In order to fit the intensities expected near the fault trace, all areas within 0.2 km of the surface expression of the fault have been assigned the highest intensity. From a practical standpoint, the remaining areas where the revised model underestimates the 1906 intensities are not significant unless the area has an intensity increment less than 0.5 (in effect, soft rock). Larger intensity increments raise the estimated intensity above $I_{1906} = 3.0$. See Plates 1a and 1b.

We note the similarity between equation 10 and the relationship determined by Borcherdt et al. (1975)

$$\delta I = 0.19 + 2.97\log(AHSA)$$

Equation 11

for the intensity increment δI associated with the average horizontal spectral amplification *AHSA* obtained from all the recording sites in the Bay Area at which there were intensity estimates for the 1906 earthquake. The coefficient of 3.0 in equation 10 is essentially the same as the coefficient 2.97. Since the average acceleration spectral level Ξ is modified linearly by the average horizontal spectral amplification, that is, $I + \delta I \propto 3.0\log(AHSA * \Xi)$, the coincidence of these two coefficients indicates that the fit obtained in Figure 4 is not fortuitous, and that intensity is proportional to the logarithm of the cube of the ground motion.

Finally, it is possible to quantify the proportionality in equation 5 and estimate the average acceleration spectral level, or equivalently, the undamped velocity response spectrum. By combining equation 5 with equation 15 in Boatwright (1982), taking averages of the various components of the high-frequency radiation pattern in equation 2 of Boatwright (1982), and assuming ρ = 2.7 gm/cm^3, β = 3.5 km/s at depth, $\Delta v = 0.8\beta$ = 2.8 km/s, $\Delta\sigma$ = 150 bars, ρ = 2.0 gm/cm^3 and β = 0.8 km/s for Franciscan sandstone, we obtain the simple relation

$$|\ddot{u}| \cong 20\Xi \text{ cm/s} \qquad \textit{Equation 12}$$

where Ξ is calculated in equation 5 with $\Delta\sigma = 1$. Combining this relation with equation 10 gives estimates of the average acceleration spectral level, or equivalently, the undamped velocity response spectrum, associated with the MMI and 1906 intensity levels, as shown in Table 1.

TABLE 1. Approximate Relationships Among Intensity Scales and Average Acceleration Spectral Level
NOTE - Average acceleration spectral level is equivalent, but not identical, to undamped velocity response spectra, as discussed in the text. It has units of velocity, not acceleration. The values are consistent with, but not identical to, the values used in other MMI maps, such as ShakeMap. The largest discrepancy is with MMI X, which rarely occurs.

Modified Mercalli Intensity	San Francisco Intensity	Average Acceleration Spectral Level
XII - Massive Destruction		(MMI XII - not shaking related)
XI - Utilities Destroyed	A - Very Violent	
X - Most Small Structures Destroyed		450 cm/sec
	B - Violent	300 cm/sec
IX - Heavy Damage		204 cm/sec
	C - Very Strong	141 cm/sec
VIII - Moderate to Heavy Damage		96 cm/sec
	D - Strong	66 cm/sec
VII - General Nonstructural Damage		45 cm/sec
	E - Weak	30 cm/sec
VI - Felt by All, Books Off Shelves		21 cm/sec
	< E - Very Weak	15 cm/sec
V - Wakes Sleepers, Pictures Move		9 cm/sec

Testing the Intensity Model by Comparing Actual Versus Predicted Red-Tagged Housing Units in Past Bay Area Earthquakes

The key test for any mapping scheme which proposes to predict the intensity patterns of future earthquakes is its ability to accurately "model" intensity patterns in past earthquakes. In the case of these maps, the principal comparison was made not with the modified Mercalli intensity map published for the Loma Prieta earthquake (Stover et al., 1990), but with actual housing damage patterns from that earthquake as measured by red-tagged dwelling units of various construction types. These units are in buildings which were "red-tagged" as being unsafe to occupy using a set of criteria published by the California Office of Emergency Services and used fairly uniformly by all of the city and county building inspection departments.

The testing process involved a comparison of predicted red-tagged units to actual red-tagged units. First, alternative models to predict intensity patterns in the Loma Prieta earthquake were generated using either the attenuation relationship of Borcherdt et al. (1975) without magnitude scaling or directivity, or the model based on the average acceleration spectral level. A second model was then run for each resulting intensity map to predict the number of red-tagged units. This second model uses estimates of the existing land use, the housing stock, and the damage matrices that relate the percent of red-tagged units by construction type to the intensity. These predictions are then systematically compared with the actual red-tagged unit counts for that earthquake for twelve building types, for each of the cities and counties in the region. The error analysis consisted of calculating the mean absolute error (MAE) and root mean square error (RMSE) for the county/ building type and community data. These error measurements were used rather than the percentage error due to the large number of zero values in the data when no actual red-tagged units were present.

This testing process was a reiterative exercise; actual red-tagged units were compared with revised predictions for the number of those units based on increasingly sophisticated assumptions about the role of directivity and the additional complication of the propagation effect associated with the Mohorovicic discontinuity (the boundary between the crust and the mantle), as well as on improved data on existing land use and building construction/unit counts for the time of the Loma Prieta earthquake. A total of over seventy models were run for this earthquake.

The two models with the "best" fit were used to create a revised matrix relating intensity percent red-tagged by modified Mercalli intensity by construction type based on the actual damage data from the Loma Prieta earthquake to predict red-tagged units. This "modified" matrix was then used to estimate the red-tagged units again, reducing the errors even further. However, the changes in the matrix were

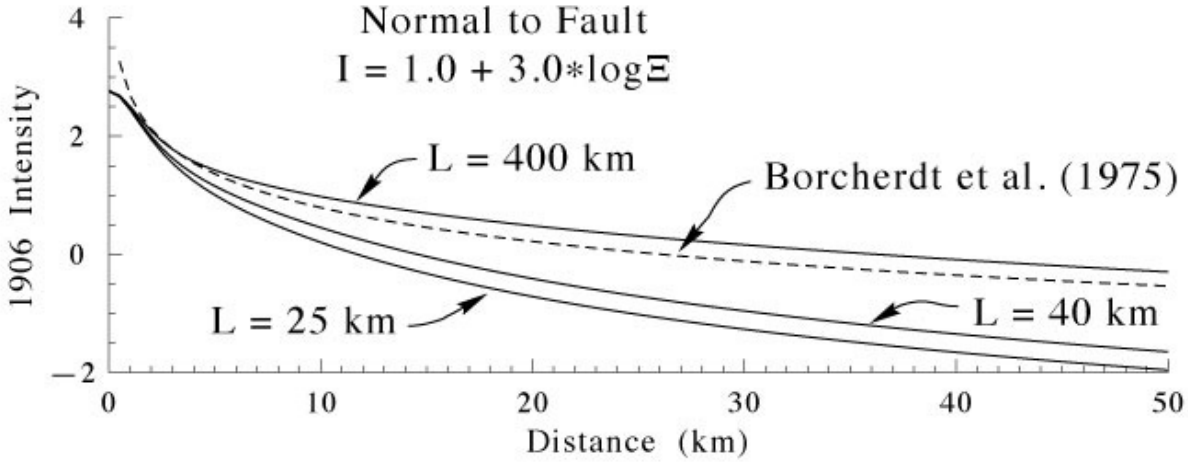

FIGURE 4. The attenuation normal to the fault for three different rupture lengths (L = 200, 40, and 25 km). These rupture lengths correspond roughly to the 1906 San Francisco earthquake, the 1989 Loma Prieta earthquake, and the 1984 Morgan Hill earthquake. The dashed line shows the fit obtained by Borcherdt et al. (1975) to the 1906 intensities. The smaller the fault length, the more rapidly the intensity attenuates away from the fault.

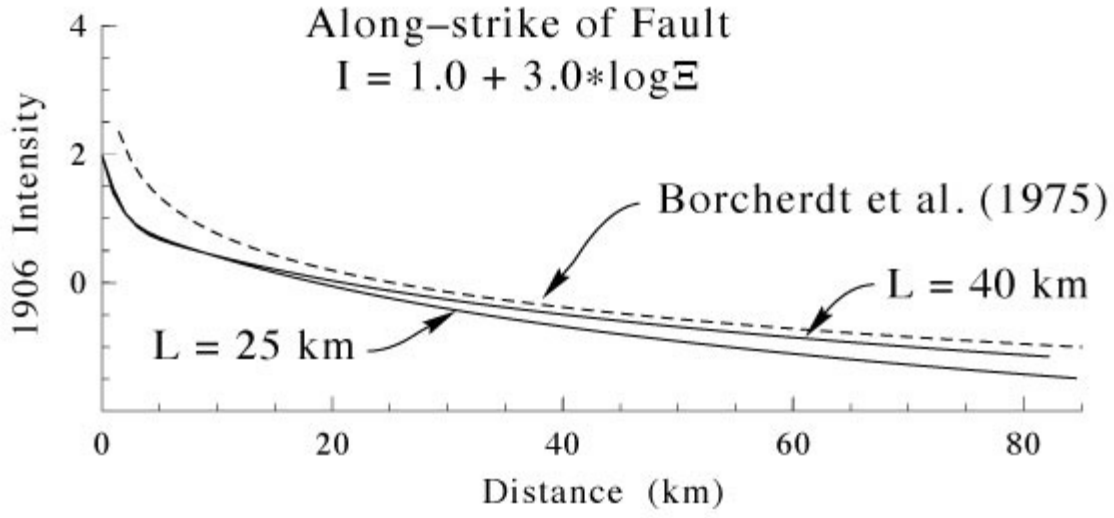

FIGURE 5. The attenuation along the fault for two different rupture lengths (L = 40 and 25 km). The dashed line shows the fit obtained by Borcherdt et al. (1975) to the 1906 intensities normal to the San Andreas fault. The attenuation of intensity as a function of distance along strike of the fault does not depend strongly on the fault length.

conservative, reflecting our respect for the quality of the data from earlier earthquakes that went into the original matrix.

The baseline error analysis using the revised damage matrix run for the "original" model (from Perkins, 1992, based on the closest point to the surface expression of the fault and the attenuation relationship of Borcherdt et al., 1975), yielded a MAE of 34.88 units by city area. This model overestimated the red-tagged units in Santa Clara County by one-third and underestimated the red-tagged units in San Francisco by a factor of twelve. The MAE was increased when a Moho "bounce" of one intensity unit was added for distances above 50 km from the end of the fault (to 37.01), but decreased (to 29.52) when a bounce of one-half an intensity unit was used.

The best fit was obtained by using the trilateral directivity model for the average acceleration spectral level in equation 5 and a Moho bounce for distances from 70 to 90 km from the end of the fault. Using $v = 0.8\beta$ as the horizontal rupture velocity and a Moho bounce of one intensity unit yields approximately the same MAE (27.80 units by city area) as $v = 0.85\beta$ and a Moho bounce of half an intensity unit (27.58). Although the damage data from Santa Cruz and San Benito Counties were not included in this analysis, the cities of Watsonville and Hollister, which lie along the fault strike to the southeast, also had higher than expected damage.

In addition, because the source model used for this mapping incorporates updip directivity, it agrees with the strong evidence for increased damage near the (unruptured) fault trace. The near-fault area exposed to modified Mercalli intensities IX and X is dominated by single family homes built prior to 1940. Over one-third of these homes were red-tagged, while only 2% of similar homes exposed to MMI VIII were red-tagged. Both the original model of Perkins (1992), based on the attenuation relationship of Borcherdt at al. (1975), and the model derived in this Appendix fit this near-fault damage.

An improvement of the model derived in this Appendix is the simultaneous decrease of the predicted number of wood-frame dwellings and mobile homes damaged in Santa Clara County and increase of the predicted number of damaged units in Oakland and San Francisco. The original model of Perkins (1992) based on the attenuation relationship of Borcherdt et al. (1975) overpredicts the damage in Santa Clara County. See Plates 2a and 2b for a comparison of the outputs of these two models.

The directivity model was then tested for a much smaller earthquake, the Morgan Hill earthquake of 1984. This $\boldsymbol{M} = 6.4$ earthquake is at the lower end of the magnitude scale of the scenario earthquakes to be modeled. The trilateral-rupture model predicted a total of 202 red-tagged units, larger than the 39 units that were actually red-tagged, but much smaller than the 1089 red-tagged units predicted by the original model. For this fit, we used a trilateral- rupture model with $v = 0.8\beta$. The Morgan Hill earthquake ruptured predominately from northwest to southeast (Beroza and Spudich, 1988). A source model with more directivity to the southeast than the northwest would yield a better fit to the number of red-tagged units. See Plates 3a and 3b for a comparison of the output of the two models.

Another recent moderate earthquake was the 1980 Livermore earthquake. The role of directivitiy in this earthquake has previously been examined by Boatwright and Boore (1982).

Conclusion

The exercise of fitting the damage associated with the 1906 San Francisco earthquake, the 1989 Loma Prieta earthquake and the 1984 Morgan Hill earthquake clearly indicates that the intensity models developed in the mid-1970s that ABAG has been using, with minor modifications, for almost twenty years have been improved by including directivity. In particular, the fit to the 1989 Loma Prieta damage provides a critical test of these intensity models, improving our ability to predict intensities for areas lying along strike from these large scenario earthquakes.

An additional improvement is the magnitude scaling derived from the physical model of the source. This scaling allows intensities to remain high near the fault, while falling off more abruptly perpendicular to the fault as the magnitude decreases. The steepness of this fall-off is less pronounced along the fault strike. These effects are significant for the range of magnitudes associated with expected future damaging earthquakes in the Bay Area.

TECHNICAL APPENDIX B -- OCCURRENCE OF AND AVERAGE PREDICTED INTENSITY INCREMENTS FOR THE GEOLOGIC UNITS IN THE SAN FRANCISCO BAY AREA

The average predicted intensity increments for the geologic units in the San Francisco Bay Area are based on the properties of the materials contained in those units. The predicted intensity increments from Table B1 are averaged for each geologic unit listed in Table B3 based on those materials.

These intensity increments (δI or fractional changes in intensity) are added to (or subtracted from) intensities calculated from the distance/directivity relationship described in Appendix A to generate the intensity map.

TABLE B1-- SEISMICALLY DISTINCT UNITS AND PREDICTED INTENSITY INCREMENTS

[modified from Borcherdt, Gibbs and Fumal (1978) based on additional shear wave velocity (v) measurements in Borcherdt and Glassmoyer (1992) and the amplification formula in Borcherdt (1994) of $F_v = (1050\ m/s/v)^{0.65}$. Then the formula $\delta I = 0.19 + 2.97 \log (F_v)$ from Borcherdt et al. (1975) was used to convert amplification to intensity increments.]

Seismic Unit for Sediments	Material Properties	Predicted Intensity Increment
I	Clay and silty clay, very soft to soft	**2.4**
II	Clay and silty clay, medium to hard	**1.8**
III	Sand, loose to dense	**1.6**
IV	Sandy clay-silt loam, interbedded coarse and fine sediment	**1.4**
V	Sand, dense to very dense	**1.1**
VI	Gravel	**0.7**

Seismic Unit for Bedrock	Rock Type	Hardness	Fracture Spacing	Predicted Intensity Increment
I	Sandstone	Firm to soft	Moderate and wider	**1.0**
II	Igneous rocks, Sedimentary rocks	Hard to soft	Close to very close	**0.7**
III	Igneous rocks, Sandstone, Shale	Hard to firm	Close	**0.5**
IV	Igneous rocks, Sandstone	Hard to firm	Close to moderate	**0.3**
V	Sandstone, Conglomerate	Firm to hard	Moderate and wider	**0.2**
VI	Sandstone	Hard to quite firm	Moderate and wider	**0**
VII	Igneous rocks	Hard	Close to moderate	**-0.2**

TABLE B2 -- SOURCE MAP REFERENCES BY AREA

Area	Author	Source Map Scale
All Flatlands Areas (except in San Mateo County)	Burke, Helley, and others, 1979	1:125,000
Northwest Area	Blake, Smith, and others, 1971	1:62,500
North Central Area	Fox, Sims, and others, 1973	1:62,500
Northeast Area	Sims, Fox, and others, 1973	1:62,500
Central Marin Area	Blake, Bartow, and others, 1974	1:62,500
Central East Area	Brabb, Sonneman, and others, 1971	1:62,500
East Bay Area	Dibblee, 1972 to 1981	1:24,500
Southeast Area	Cotton, 1972	1:62,500
Southwest Santa Clara Area	Brabb and Dibblee, 1978 to 1980	1:24,500
Northwest Santa Clara Area	Brabb, 1970	1:62,500
San Mateo Area	Brabb and Pampeyan, 1983	1:62,500
South San Francisco Area	Bonilla, 1971	1:24,000
North San Francisco Area	Schlocker, Bonilla and Radbruch, 1958	1:24,000
West Alameda Area	Brabb, unpublished	1:62,500
Oakland Area	Radbruch, 1957 and 1969	1:24,000

FIGURE -- SOURCE MAP AREAS FOR GEOLOGIC INFORMATION
(using a USGS 7.5' quadrangle index map as a base map)

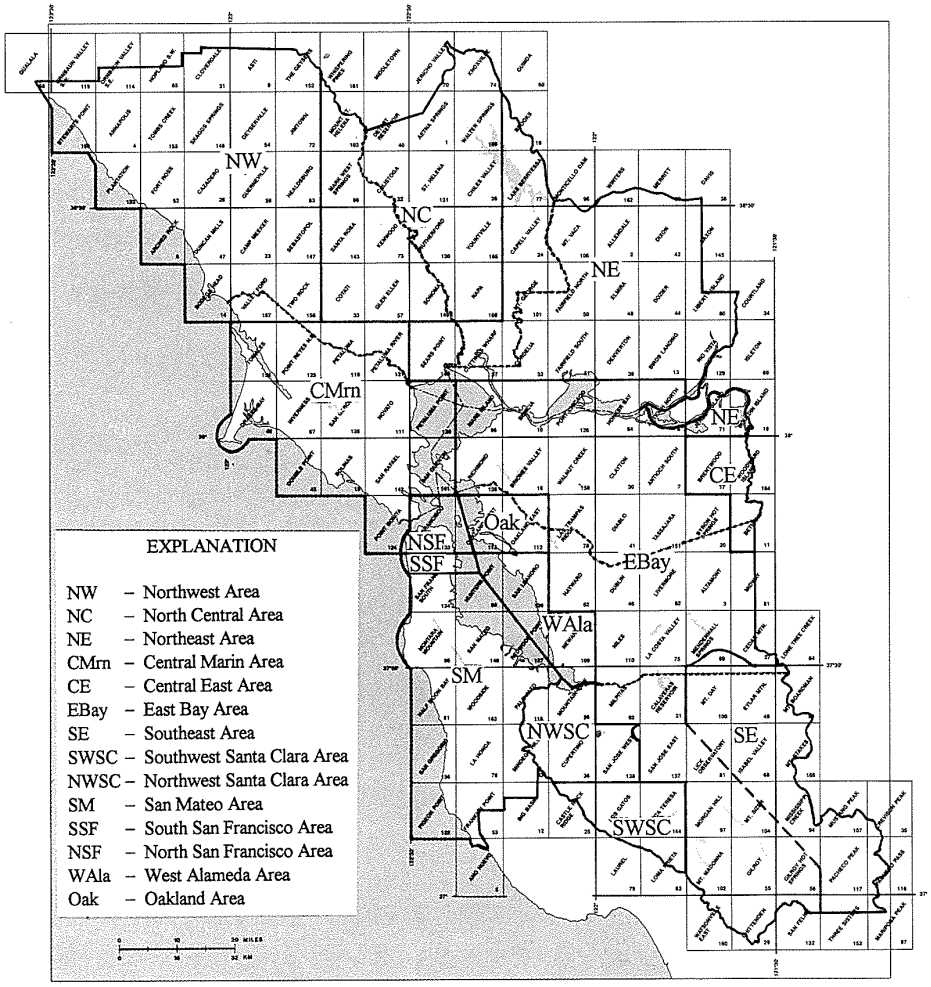

TABLE B3 -- OCCURRENCE OF AND AVERAGE PREDICTED INTENSITY INCREMENTS FOR THE GEOLOGIC UNITS IN THE SAN FRANCISCO BAY AREA

[Seismic units present are modified and expanded from Fumal (1978) based on pers. comm. with T. Fumal and J. Gibbs (1978 to 1983) and data on Merritt sand in Borcherdt and Glassmoyer (1992). The strategraphic nomenclature and unit age assignments used in this table may not necessarily conform to current usage by the U.S. Geological Survey.]

Map Symbol (s)	Geologic Unit	Source Map	Seismic Units Present	Average Predicted Intensity Increment
Quaternary Units				
1. Qu	Undivided Quaternary alluvium (due to occurrence in urban areas)	Flat	II, III, IV, V, VI	1.3
2. Qhaf (purple); Qaf	Artificial fill	Flat; CE; SM	II, III, V	1.5
3. Qhsc; Qal	Holocene stream channel deposits	Flat; SM	III, V	1.4
4. Qhac; Qyf	Holocene coarse-grained alluvium; fan and basin deposits	Flat; SM	V	1.1
5. Qham; Qyfo	Holocene medium-grained alluvium; fan and plain deposits	Flat; SM	III	1.6
6. Qhaf; Qb	Holocene fine-grained alluvium; fan and plain (basin) deposits	Flat; SM	II	1.8
7. Qhafs	Holocene fine-grained alluvium; fan and plain (basin) deposits--salt-affected	Flat	II	1.8
8. Qhbm; Qm	Holocene Bay mud	Flat; SM	I	2.4
9. Qcl	Holocene colluvium; slope wash and ravine fill	SM; data gaps	III, V	1.4
10. Qhs; Qs	Holocene beach and windblown sand	Flat; SM	III, V	1.4
11. Qpa	Pleistocene alluvium	Flat	V, VI	0.9
12. Qps	Pleistocene sand; Merritt sand	Flat	II	1.8
13. Qpea	Early Pleistocene alluvium	Flat	V, VI	0.9
14. Qof	Pleistocene coarse-grained alluvium; fan deposits	SM	V, VI	0.9
15. Qob	Pleistocene fine-grained alluvium; basin deposits	SM	II, IV	1.6
16. Qpmt; Qmt	Pleistocene marine terrace deposits	Flat; SM	V	1.1
17. Qm	Quaternary Montezuma Formation	NE	V	1.1
18. Qr	Quaternary tuff and gravel from rhyolite	NC; NE, CMrn	V, VI	0.9
19. Qg	Quaternary gravel, poorly bedded	NC	V, VI	0.9
20. Qg	Quaternary stream gravel and sand	EBay; SWSC	III, V	1.4
21. Qr	Quaternary rhyolite of the Clear Lake area	NW; adj. area on NC	III, VII	0.2
22. Qclt	Quaternary Clear Lake area tuff	NW; NC	I, II	0.8
23. Qob	Quaternary olivine basalt of Clear Lake area	NC	II, VII	0.2
24. Qmi	Quaternary Millerton Formation	CMrn	III, VI	1.2
25. Qpmc; Qc	Quaternary Colma Formation	Flat; CMrn; SSF; NSF	V	1.1
26. Qlv	Quaternary boulder gravels of volcanic debris	EBay	VI	0.7
Quaternary/Tertiary Units				
27. QTs; Qsc	Santa Clara Formation	EBay; SWSC; SM; NWSC	III, IV, V, VI, V, VII	0.8
28. Qsb	Santa Clara Formation--gravel with basalt detritus	EBay	V, VI	0.9
29. Qsp	Santa Clara Formation--conglomerate or breccia detritus	EBay	VI	0.7
30. Qsa	Santa Clara Formation--clay	EBay	III	1.6
31. Qsc w/a	Santa Clara Formation--andesite	EBay	VII	-0.2
32. Qsc w/b	Santa Clara Formation--basalt	EBay	VII	-0.2
33. QThg	Huichica and Glen Ellen Formation	NC; NE	VI, I	0.8
34. QTge	Glen Ellen Formation	NW	VI, I	0.8
35. QTget	Glen Ellen Formation with tuff	NW	VI, I	0.8
36. QTc	Cache Formation	NC	I	1.0
37. QTl	Livermore Gravel	EBay	III, IV, V, VI	1.2
38. QTt	Tassajara Formation	EBay	III, IV, V	1.4
39. QTb	Unnamed olivine basalt lava	EBay	VII	-0.2
40. bi	Intrusive basalt in QTb	EBay	VII	-0.2
41. QTp	Paso Robles Formation	EBay	II, V, VI	1.2
42. Qtm; Tm; Tme (?)	Merced Formation	NW; NC; CMrn; SM; SSF; NWSC	I	1.0

Map Symbol (s)	Geologic Unit	Source Map	Seismic Units Present	Average Predicted Intensity Increment
Tertiary Units (Pliocene)				
43. Tp	Pliocene Purisima Formation--undivided	EBay; SWSC; SM	I, II	0.8
44. Tptu	Pliocene Tunitas Sandstone Member of the Purisima Fm.	SM	I, II	0.8
45. Tpl	Pliocene Lobitos Mudstone Member of the Purisima Fm.	SM	I	1.0
46. Tpsg	Pliocene San Gregorio Sandstone Member of the Purisima Formation	SM	I, II	0.8
47. Tpp	Pliocene Pomponio Siltstone Member of the Purisima Fm.	SM	II, III	0.6
48. Tpt	Pliocene Tehama Sandstone and Siltstone Member of the Purisima Formation	SM	I, II	0.8
49. Tor	Pliocene Ohlson Ranch Formation	NW	I	1.0
50. Tors	Pliocene Ohlson Ranch Formation--sandstone	NW	I	1.0
51. Torc	Pliocene Ohlson Ranch Formation--conglomerate	NW	IV	1.4
52. Tpt	Pliocene Tuff of Putah Creek	NE	I, II	0.8
53. Tlt; Tpl	Pliocene Lawlor Tuff	NE	I, II	0.8
54. Tp	Pliocene Petaluma Formation--undivided	NC	I, II	0.8
55. Tps	Pliocene Petaluma Fm.--claystone, siltstone and mudstone	NE; CMrn	I, II	0.8
56. Tpc	Pliocene Petaluma Formation--imbedded gray claystone	NE; CMrn	I, II	0.8
57. Tp (?)	Pliocene Petaluma Formation--questionable	NW	I, II	0.8
58. Tsv	Pliocene Sonoma Volcanics--undivided	NE; CMrn	I, II, III, VII	0.5
59. Tsr	Pliocene Sonoma Volcanics--rhyolitic lava flows	NC; NE; CMrn	IV, V, VI, VII	0.1
60. Tsri	Pliocene Sonoma Volcanics--rhyolitic plugs and dikes	NC; NE; CMrn	II, III, VII	0.3
61. Tsrs	Pliocene Sonoma Volcanics--soda rhyolite flows	NC	VII	-0.2
62. Tsrp	Pliocene Sonoma Volcanics--perlitic rhyolite	NC; NE	VII	-0.2
63. Tsrb	Pliocene Sonoma Volcanics--rhyolitic breccia	NW; NC	VII	-0.2
64. Tsa	Pliocene Sonoma Volcanics--andesitic to basaltic lava flows	NC; NE; CMrn	III, VII	0.2
65. Tsai	Pliocene Sonoma Volcanics--andesitic to dacitic plugs	NC; NE	VII	-0.2
66. Tsfd	Pliocene Sonoma Volcanics--basaltic or andesitic lava flows with diatomite	NC	I, VII	0.4
67. Tsb	Pliocene Sonoma Volcanics--basalt	NW	VII	-0.2
68. Tst	Pliocene Sonoma Volcanics--pumicitic ash-flow tuff	NC; NE; CMrn	I, II, VII	0.5
69. Tswt	Pliocene Sonoma Volcanics--welded ash-flow tuff	NC; NE	II, VII	0.2
70. Tstx	Pliocene Sonoma Volcanics--tuff (?), welded, massive, hard, xenolithic	NC	VII	-0.2
71. Tsag	Pliocene Sonoma Volcanics--agglomerate	NC; NE	II, III	0.6
72. Tslt	Pliocene Sonoma Volcanics--tuff breccia	NC; NE	II, III, VI	0.4
73. Tsft	Pliocene Sonoma Volcanics--pumicitic ash-flow tuff with lava flows	NC	I, II, VII	0.5
74. Tss	Pliocene Sonoma Volcanics--sedimentary deposits	NC; NE	VI, I, II	0.8
75. Tssd	Pliocene Sonoma Volcanics--diatomite	NC; NE	I, II, VI	0.6
76. rh	Pliocene rhyolite; includes the Alum Rock Rhyolite and Leona Rhyolite	EBay; Oak; WAla	III, IV, V, VI, VII	0.2
77. Tb; Tbu	Pliocene unnamed basalt; included basalt in the Orinda Fm.	EBay	II, VI	0.4
78. Tri	Pliocene rhyolitic intrusive	EBay	VII	-0.2
79. a	Pliocene andesitic rock	EBay	VII	-0.2
80. Tpb	Pliocene Putnam Peak Basalt	NE	VII	-0.2
81. Tcu	Pliocene Contra Costa Group--undivided	Oak	I, II, IV	0.7
82. Tbp	Pliocene Bald Peak Basalt	EBay; Oak	II, VII	0.2
83. Ts	Pliocene Siesta Formation	Oak	II, III, IV	0.6
84. Tmb	Pliocene Moraga Formation--basalt and andesite	EBay; Oak	VI, VII	-0.1
85. Tmt; Tmc	Pliocene Moraga Fm.--clastic rocks, including tuff breccia	EBay; Oak	II, III	0.6
86. Tps; Tor; Tw; Tpo; Tpth; Tol; Tsc	Pliocene non-marine sedimentary rocks, locally called the Orinda, Wolfskill, Tehama or Oro Loma	NE; CE; EBay; Oak	I, II, III, IV, V	0.5
87. Tpl	Pliocene lacustrine limestone	EBay	VI	0.0
88. Tpt	Pliocene tuff and sandstone, including the Pinole Tuff	EBay	III, VI	0.2

Map Symbol (s)	Geologic Unit	Source Map	Seismic Units Present	Average Predicted Intensity Increment
89. Tpc; Tuc	Pliocene non-marine sedimentary rocks, clay with sandstone and conglomerate	EBay	VI, I, II	0.8
90. Tcg	Pliocene non-marine pebble conglomerate	EBay	VI	0.7
91. Tus	Pliocene non-marine sandstone	EBay	II, IV	0.5
92. Te	Pliocene Etchegoin Formation	EBay	I, II	0.8
Tertiary Units (Plicene/Miocene)				
93. Tsc	Pliocene/Miocene Santa Cruz Mudstone	SM	II, III	0.6
94. Tsm	Pliocene/Miocene Santa Margarita Sandstone	SM	I, II	0.8
95. Tvia; Tv	Pliocene/Miocene Quien Sabe Volcanics--intrusive andesitic rocks	EBay; SE	VII	-0.2
96. Tpx	Pliocene/Miocene sandstone--probably a large clastic dike	CMrn	VI	0.0
97. Tdbc	Pliocene/Miocene Drakes Bay siltstone and mudstone	CMrn	II, III	0.6
98. Tdbs	Pliocene/Miocene Drakes Bay glaucomitic sandstone	CMrn	I, II	0.8
Tertiary Units (Miocene)				
99. Tsm	Miocene sandstone and mudstone in Skaggs and Duncans Mills quadrangles	NW	I, II	0.8
100. Tn, Tmn	Miocene Neroly Sandstone	NE; CE; EBay	I, II	0.8
101. Tn (?)	Miocene questionable Neroly Sandstone	NC	I, II	0.8
102. Tmss; Tmb, Tbr; Tmci	Niocene sandstone, including the Cierbo and Briones Formations	NE; EBay	IV, VI	0.2
103. Tmbu	Miocene Briones Sandstone--upper member (sandstone)	NE	IV, V, VI	0.2
104. Tmbm	Miocene Briones Sandstone--middle member (light gray siliceous shale)	NE	II, III	0.6
105. Tmbl	Miocene Briones Sandstone--lower member (sandstone)	NE	IV, V, VI	0.2
106. Tmsl	Miocene siltstone with minor sandstone	EBay	III, IV	0.4
107. Tms	Miocene unnamed sandstone, siltstone and shale	NC	II	0.7
108. Tmc	Miocene non-marine clay	EBay	II	0.7
109. Tmsa	Miocene tan fine-grained sandstone, local basal conglomerate	EBay	II, IV	0.5
110. Ttv	Miocene dacite and rhyolite dacite tuff breccia	SWSC	III, IV, VII	0.2
111. Tus	Miocene unnamed sandstone	SM; NWSC	I	1.0
112. Tmsh; Tmc; Tma; Tm	Miocene silty-siliceous gray shale (including the Monterey Shale & upper Claremont Shale)	EBay; SWSC; SM; NWSC	II, III	0.6
113. Tt	Miocene Tice Shale	Oak	II, III, V	0.5
114. Tmsc; Tmi	Miocene brittle cherty-siliceous shale (including the Claremont Shale and lower Claremont Shale)	EBay; Oak	II, III, IV	0.5
115. Tms; Tmso	Miocene basal sandstone (including the Sobrante Sandstone & Temblor Sandstone)	EBay; SWSC; Oak	IV, V, VI	0.2
116. Ts; Tmsr	Miocene sandstone (including the San Ramon Formation)	NE; EBay	III, IV	0.4
117. Tpm	Miocene Page Mill Basalt	SM; NWSC	III, IV, V, VI, VII	0.2
118. Tmsu	Miocene unnamed graywacke sandstone	EBay	I, II	0.8
Tertiary Units (Miocene/Oligocene)				
119. Tuv	Miocene/Oligocene unnamed volcanic rocks	SM	III, IV, V, VI, VII	0.2
120. Tls	Miocene/Oligocene Lambert Shale and San Lorenzo Fm.	SM; NWSC	I	1.0
121. Tla	Miocene/Oligocene Lambert Shale	SWSC; SM; NWSC	II, III	0.6
122. Tmb	Miocene/Oligocene Mindego Basalt and related volcanic rocks	SM; NWSC	III, IV, V, VI, VII	0.2
123. Tlo	Miocene/Oligocene Lompico Sandstone	SWSC; SM	V	0.2
124. Tvq	Miocene/Oligocene Vaqueros Sandstone	SWSC; SM; NWSC	V	0.2
125. Tb	Miocene/Oligocene basalt and diabase flow and sills	SWSC; SE	VII	-0.2
126. Tui	Miocene/Oligocene unnamed marine shale--siliceous and clay shale	EBay	II, III	0.6
127. Tuc	Miocene/Oligocene unnamed marine shale--clay shale and minor sandstone	EBay	II, III	0.6
Tertiary Units (Oligocene)				
128. Tkt	Oligocene Kirger Formation--tuff	EBay	II	0.7
129. Tks	Oligocene Kirger Formation--tuffaceous sandstone	EBay	I, II	0.8

Map Symbol (s)	Geologic Unit	Source Map	Seismic Units Present	Average Predicted Intensity Increment
Tertiary Units (Oligocene/Eocene)				
130. Tsl	Oligocene/Eocene San Lorenzo Formation	SWSC; SM; NWSC	I	1.0
131. Tsr	Oligocene/Eocene Rices Mudstone Member of the San Lorenzo Formation	SWSC; SM; NWSC	I	1.0
132. Tst	Oligocene/Eocene Twobar Shale Member of the San Lorenzo Formation	SWSC; SM	I	1.0
Tertiary Units (Eocene)				
133. Tb	Eocene Butano Sandstone south of La Honda	SWSC; SM; NWSC	II, III, IV, V, VI	0.3
134. Tb	Eocene Butano Sandstone north of La Honda	SM	II, III, IV, V, VI	0.3
135. Tbs	Eocene shale in the Butano Sandstone	SWSC; SM	I	1.0
136. Tb?	Eocene Butano Sandstone--questionable	SM; NWSC	I	1.0
137. Tt	Eocene Tolman Formation--sandstone and siltstone	EBay	IV, V	0.2
138. Tk	Eocene Kreyenhagen Formation	NE; EBay	I, II	0.8
139. Tksh	Eocene Kreyenhagen Formation--semi-siliceous shale	NE; EBay	II	0.7
140. Tkm; Tem, Tmk	Eocene Markley Sandstone of Kreyenhagen Formation	NE; CE; EBay	I, II	0.8
141. Tems; Tmu	Eocene Markley Sandstone of Kreyenhagen Formation--Upper sandstone unit	NE; EBay	I, II	0.8
142. Tml	Eocene Markley Sandstone of Kreyenhagen Formation--lower sandstone unit	CE	I, II	0.8
143. Tkn; Tnv	Eocene Nortonville Shale of Kreyenhagen Formation	NE; CE; EBay	II	0.7
144. Tenu	Eocene Nortonville Shale of Kreyenhagen Formation--upper shale unit	NE	II	0.7
145. Tenm	Eocene Nortonville Shale of Kreyenhagen Formation--middle sandstone unit	NE	II, V	0.4
146. Ten?	Eocene Nortonville Shale of Kreyenhagen Formation--lower shale unit	NE	II	0.7
147. Tds; Ted; Td	Eocene Domengine Sandstone--tan, arkosic	NC; NE; CE; EBay	I, V	0.6
148. Tec	Eocene Capay Formation--brown and gray shale and sandy mudstone	NE	II, III	0.6
149. Tmg	Eocene Meganos Formation--undivided; some parts queried	EBay	I, II	0.8
150. Tmge; Tme	Eocene Meganos Formation--Division E, greenish gray marine silty mudstone	CE; EBay	II	0.7
151. Tmgd; Tmd	Eocene Meganos Formation--Division D, light gray marine sandstone	CE; EBay	V, I, II	0.9
152. Tmgc; Tmc	Eocene Meganos Formation--Division C, bluish gray marine shale; many sandstone interbeds locally mapped	CE; EBay	I, II	0.8
153. Tmgs; Tmcs	Eocene Meganos Formation--sandstone interbeds locally mapped within Division C	EBay	I, II	0.8
154. Tmga; Tma	Eocene Meganos Formation--Divisions A and B, basal grayish brown marine sandstone	CE; EBay	I, II	0.8
155. Tmgs	Eocene sandstone within Meganos Formation	EBay	I, II	0.8
156. Tts	Eocene Tesla Formation	EBay	II	0.7
157. Tss	Eocene Tesla Formation--medium-grained sandstone, minor clay shale	EBay	II	0.7
158. Tss	Eocene unnamed sandstone and shale	Oak	II, VI	0.4
159. Tss	Eocene unnamed sandstone and shale in southwest Santa Clara County	EBay; SWSC	II, III, IV, VI	0.4
160. Tss; Ts	Eocene unnamed sandstone in SW Santa Clara County	SWSC	II	0.7
161. Tls	Eocene unnamed limestone in SW Santa Clara County	SWSC	III, IV, VII	0.2
Tertiary Units (Eocene/Paleocene)				
162. Tsh; Tssh	Eocene/Paleocene marine shale and micaceous shale in southwest Santa Clara County	EBay; SWSC	II	0.7
163. Tg	Eocene/Paleocene strata of German Rancho	NW	IV, V, VI	0.2
Tertiary Units (Paleocene)				
164. Tss	Paleocene unnamed sandstone and shale	SM	III, IV, VI	0.3
165. Tpu	Paleocene unnamed shale with sandstone	NE	II	0.7
166. Tpus	Paleocene unnamed shale--upper sandstone member	NE	II	0.7
167. Tmz	Paleocene Martinez Formation	NE; EBay	II	0.7
168. Tpmu	Paleocene Martinez Formation--upper member; silty mudstone and shale	NE	II	0.7

Map Symbol (s)	Geologic Unit	Source Map	Seismic Units Present	Average Predicted Intensity Increment
169. Tpm?	Paleocene Martinez Formation--lower member; sandstone	NE; EBay	II	0.7
170. Tp	Paleocene Pinehurst Shale	Oak	II, III	0.6
171. Tv	Paleocene Vacaville Shale of Merriam and Turner	NC	II	0.7
172. Tl	Paleocene Laird Sandstone	CMrn	IV, V, VI	0.2
173. Tpr	Paleocene conglomerate at Point Reyes	CMrn	V, VI	0.1
Tertiary (Paleocene)/Cretaceous Units				
174. TKpr	Lower Tertiary/Upper Cretaceous Pinehurst Shale and Redwood Canyon Formation	Oak	II, III, IV, V	0.4
175. TKu	Lower Tertiary/Upper Cretaceous undifferentiated sandstone, mudstone and conglomerate of Stewards Point quadrangle	NW	II, IV, V	0.4
176. TKpr	Lower Tertiary/Upper Cretaceous unnamed shale; marine clay shale and minor thin sandstone of Santa Clara County	EBay; SWSC	II, III	0.6
177. TKss	Lower Tertiary/Upper Cretaceous unnamed marine arkosic sandstone of Santa Clara County	SWSC	V, II	0.9
178. KTsh; KTs	Lower Tertiary/Upper Cretaceous unnamed micaceous clay shale, siltstone	EBay; SE	II, III	0.6
179. KTs	Lower Tertiary/Upper Cretaceous sandstone within unnamed shale, siltstone	EBay	III, IV, V	0.3
180. KTsh with circles	Lower Tertiary/Upper Cretaceous conglomerate within unnamed shale, siltstone	EBay	V	0.2
181. KTsh with dashes	Lower Tertiary/Upper Cretaceous limestone within unnamed shale, siltstone	EBay	VI	0.0
Cretaceous Units				
182. Ku	Upper Cretaceous rocks, undivided Great Valley Sequence	Oak	II, III, IV, V	0.4
183. Kss	Upper Cretaceous marine sandstone and shale in southwest Santa Clara County	SWSC	II, III, VI	0.4
184. Ksh	Upper Cretaceous marine micaceous shale in southwest Santa Clara County	SWSC	IV, V, VI	0.2
185. Kcg	Upper Cretaceous marine pebble conglomerate in southwest Santa Clara County	SWSC	V, VI	0.1
186. Kcg	Cretaceous conglomerate and sandstone, unnamed	EBay	V, VI	0.1
187. Ksh	Cretaceous dark shale, unnamed	EBay	II, III	0.6
188. Ka	Cretaceous strata of Anchor Bay	NW	II, IV, VI	0.3
189. Ks	Cretaceous strata of Stewards Point	NW	II, IV, VI	0.3
190. Ksb	Cretaceous spilite (sodic basalt) near Black Point on Stewards Point quadrangle	NW	VII	-0.2
191. Kpp	Cretaceous Pigeon Point Formation	SM	V, VI	0.1
192. Kgr	Cretaceous granitic rocks of Montara Mountain	SM	VII	-0.2
193. Kgr	Cretaceous granitic rocks at Bodega Head	NW	VII	-0.2
194. gr; Kgr	Cretaceous granitic rocks in Marin County	CMrn	VII	-0.2
195. Ksh	Cretaceous unnamed shale	SM	I	1.0
196. KJgv	Cretaceous/Jurassic Great Valley Sequence undifferentiated	NW	II, III, IV, V	0.4
197. Km	Cretaceous Great Valley Seq. Moreno Shale--clay shale	CE; EBay	II, III	0.6
198. Kms	Cretaceous Great Valley Seq. Moreno Shale--sandstone	CE; EBay	II, VI	0.4
199. Kmi	Cretaceous Great Valley Sequence Moreno Shale--semi-siliceous shale	EBay	II, III	0.6
200. Kps (also Kj)	Cretaceous Great Valley Sequence Panoche Formation buff arkosic sandstone, minor shale	CE; EBay	III, IV, V, VI	0.2
201. Kpc	Cretaceous Great Valley Sequence Panoche Formation--cobble conglomerate and sandstone	EBay	V, VI	0.1
202. Kp (also Kmu)	Cretaceous Great Valley Sequence Panoche Formation--micaceous shale, minor thin sandstone beds	CE; EBay	II, III	0.6
203. Kpl	Cretaceous Great Valley Sequence Panoche Formation--marine clay shale, minor sandstone	EBay	IV, V	0.2
204. Kdv	Cretaceous Great Valley Sequence Deer Valley Formation--arkosic sandstone	CE; EBay	IV, V	0.2

Map Symbol (s)	Geologic Unit	Source Map	Seismic Units Present	Average Predicted Intensity Increment
205. Ks	Cretaceous Great Valley Seq. unnamed marine clay shale	EBay	IV, V	0.2
206. Ksh	Cretaceous Great Valley Sequence marine micaceous shale, undivided	EBay	II, III, IV	0.5
207. Kcg; cg	Cretaceous Great Valley Sequence conglomerate younger than marine shale	EBay	V	0.2
208. Kshu	Cretaceous Great Valley Seq. Berryessa Fm., undivided	EBay	III, IV, V, VI	0.2
209. Kshb	Cretaceous Great Valley Sequence shale within the Berryessa Formation	EBay; SE	III, IV	0.4
210. Ksg	Cretaceous Great Valley Sequence sandstone and conglomerate within the Berryessa Formation	EBay	VI	0.0
211. Kss	Cretaceous Great Valley Sequence sandstone within the Berryessa Formation	EBay	V, VI	0.1
212. Kr	Cretaceous Great Valley Sequence Redwood Canyon Fm.	Oak	IV, V	0.2
213. Ks	Cretaceous Great Valley Sequence Shephard Creek Fm.	Oak	II, III	0.6
214. Kcg; Kcgo	Cretaceous Great Valley Sequence Oakland Conglomerate	EBay; SE; Oak	IV, V	0.2
215. Kjm	Cretaceous Great Valley Sequence Joaquin Miller Fm.	Oak	III, IV, V	0.3
216. Ku	Cretaceous Great Valley Sequence unnamed formation sandstone and shale, undivided	NE	II, III, VI	0.4
217. Kuu	Cretaceous Great Valley Sequence unnamed formation--upper sandstone member	NE	II, VI	0.4
218. Kul	Cretaceous Great Valley Sequence unnamed formation--lower shale member	NE	II, III	0.6
219. Kfo	Cretaceous Great Valley Sequence Forbes Fm. of Kirby	NE	IV	0.3
220. Kg	Cretaceous Great Valley Sequence Guida Fm. of Kirby	NE	III, V, VI	0.2
221. Kf	Cretaceous Great Valley Sequence Funks Fm. of Kirby	NE	V, VI	0.1
222. Ks	Cretaceous Great Valley Sequence Sites Fm. of Kirby	NE	III, V, VI	0.2
223. Ky	Cretaceous Great Valley Sequence Yolo Fm. of Kirby	NE	III, V, VI	0.2
224. Kv	Cretaceous Great Valley Sequence Venado Fm. of Kirby	NC; NE	VI	0.0
225. Kgvs	Cretaceous Great Valley Sequence unnamed sandstone, mudstone, shale and conglomerate	NC; NE	IV, V, VI	0.2
Cretaceous/Jurassic Units				
226. KJgvm	Cretaceous/Jurassic Great Valley Sequence unnamed fm.--mudstone, shale, siltstone, sandstone and conglomerate	NC; NE	II, III	0.6
227. KJgrs	Cretaceous/Jurassic Great Valley Sequence siltstone with minor sandstone	NW	II, III	0.6
228. KJv	Cretaceous/Jurassic unnamed volcanic rocks	SM	III, IV, V, VI, VII	0.2
229. KJs	Cretaceous/Jurassic unnamed sandstone	SM	V, VI	0.1
230. KJs	Cretaceous/Jurassic shale in SW Santa Clara County	SWSC	IV	0.3
231. KJa	Cretaceous/Jurassic argillite in SW Santa Clara County	SWSC	IV	0.3
232. Kshl; JKk	Cretaceous/Jurassic Great Valley Sequence Knoxville Formation shale with sandstone	EBay; Oak; WAla	II, III, IV	0.5
233. JKc	Cretaceous/Jurassic Great Valley Sequence Knoxville Formation conglomerate and sandstone	EBay	III, IV	0.4
234. Jk	Cretaceous/Jurassic Great Valley Sequence Knoxville Formation siltstone	NC	IV	0.3
235. Jk	Cretaceous/Jurassic Great Valley Sequence Knoxville Formation mudstone and shale	NE	IV	0.3
236. KJgvc	Cretaceous/Jurassic Great Valley Sequence Novato Conglomerate and unnamed conglomerate	NW; CMrn	IV, V	0.2
237. KJgv	Cretaceous/Jurassic Great Valley Sequence sandstone with claystone	CMrn	III, IV, V, VI	0.2
238. KJgvs	Cretaceous/Jurassic Great Valley Sequence sandstone, shale and conglomerate	CMrn	III, IV, V	0.3
239. bd	Cretaceous/Jurassic basalt and diabase	SWSC	VII	-0.2
240. vb	Cretaceous/Jurassic volcanic rocks	EBay	VII	-0.2
241. vb	Cretaceous/Jurassic basalt in SW Santa Clara County	SWSC	VII	-0.2
242. vd	Cretaceous/Jurassic diorite in SW Santa Clara County	SWSC	VII	-0.2

Map Symbol (s)	Geologic Unit	Source Map	Seismic Units Present	Average Predicted Intensity Increment
243. KJsp; Jsp	Cretaceous/Jurassic Great Valley Sequence sedimentary serpentine	NC; NE	II, III, IV	0.5
244. Jv	Jurassic basaltic pillow lava and breccia at the base of the Great Valley Sequence	NW; NC; NE	III, VI, VII	0.1
245. Jd	Jurassic diabase, gabbro, etc. at the base of the Great Valley Sequence	NW	VII	-0.2
246. Ju	Jurassic ultramafic rock at the base of the Great Valley Seq.	NW	III, VII	0.2
Cretaceous/Jurassic Franciscan Assemblage and Small Masses				
247. KJf	Cretaceous/Jurassic Franciscan Assemblage, undifferentiated	EBay; SM; NWSC; WAla	II, III, IV, V, VI, VII	0.2
248. KJfss; fs; gwy; KJfs; KJs	Cretaceous/Jurassic Franciscan Assemblage, graywacke sandstone, some local shale	NW; CMrn; EBay; SE; SM; SSF; NSF; Oak; NWSC; WAla	III, VI	0.2
249.KJsh	Cretaceous/Jurassic Franciscan Assemblage, shale with some sandstone	NSF; NWSC; WAla	III	0.5
250. KJfg; fg; gs	Cretaceous/Jurassic Franciscan Assemblage greenstone	NW; NC; NE; CMrn; EBay; SE; SM; SSF; NSF; Oak; NWSC; WAla	VII	-0.2
251. KJfm	Cretaceous/Jurassic Franciscan Assemblage metagraywacke and other metamorphic rocks	NW; NC; NE; CMrn; SE; NSF	VII	-0.2
252. KJfs; fsr; KJu	Cretaceous/Jurassic Franciscan Assemblage melange or sheared rocks	NW; NC; NE; CMrn; EBay; SE; SM; SSF; NSF; NWSC	II, III, IV, V, VI	0.3
253. fm; KJfm	Cretaceous/Jurassic Franciscan Assemblage metamorphic rocks	EBay; SM; SSF; Oak	VII	-0.2
254. br	Cretaceous/Jurassic fault (?) breccia	EBay	II, III	0.6
255. r	Cretaceous/Jurassic Franciscan Assemblage hard monolithic fragments	EBay	VII	-0.2
256. ch & gs	Cretaceous/Jurassic chert and greenstone	CMrn	III, VII	0.2
257. mch	Cretaceous/Jurassic metachert	NE	III	0.5
258. ch; fc; KJfc	Cretaceous/Jurassic Franciscan Assemblage chert	NW; NC; NE; CMrn; EBay; SE; SM; SSF; NSF; Oak; NWSC; WAla	III	0.5
259. mgs	Cretaceous/Jurassic greenstone and schistose rocks	NE	II, III, VII	0.3
260. m, pKm	Cretaceous/Jurassic and pre-Cretaceous high-grade metamorphic rocks	NW; NC; NE; CMrn; SE	IV, V, VI, VII	0.1
261. gl	Cretaceous/Jurassic glaucophane schist	EBay	III, IV, V, VI, VII	0.2
262. m	Cretaceous/Jurassic marble and hornfels	SM	IV, V, VI, VII	0.1
263. fl	Cretaceous/Jurassic Franciscan Assemblage limestone	SM; EBay; NWSC; WAla	IV, V, VI, VII	0.1
264. tr	Cretaceous/Jurassic travertine	EBay	IV, V, VI, VII	0.1
265. sc	Cretaceous/Jurassic silicacarbonate rocks	NW; NC; CMrn; EBay	III, IV, V, VI, VII	0.2
266. ////	Cretaceous/Jurassic hydrothermally altered rocks	CMrn	III, IV, V, VI	0.2
267. fcg	Cretaceous/Jurassic Franciscan Assemblage conglomerate	CMrn; SM	III, IV, V, VI	0.2
268. sp	Cretaceous/Jurassic serpentine or serpentinite	NW; NC; NE; CMrn; EBay; SE; SM; SSF; NSF; Oak; NWSC; WAla	II, III, IV, V, VI	0.3
269. spr	Cretaceous/Jurassic serpentine rubble	EBay	II, III, IV, V, VI	0.3
270. db	Cretaceous/Jurassic diabase	EBay	VII	-0.2
271. an	Cretaceous/Jurassic andesite	EBay	VII	-0.2
272. gb	Cretaceous/Jurassic gabbrodiabase	EBay; NSF; Oak	VII	-0.2
273. ##	Cretaceous/Jurassic foliate metabasalt	NW	III, VII	0.2
274. mi	Cretaceous/Jurassic mafic intrusive rocks (gabbro & diorite)	NC	VII	-0.2
275. vk	Cretaceous/Jurassic kertophyre	EBay	VII	-0.2
276. di	Cretaceous/Jurassic diorite and diabase	EBay	VII	-0.2
277. qg	Cretaceous/Jurassic hornblende quartz-gabbro	EBay	VII	-0.2